

Aberration Correcting Vision Transformers for High-Fidelity Metalens Imaging

Byeonghyeon Lee¹
Yangkyu Kim²

Youbin Kim²
Debabrata Mandal³

Yongjae Jo²
Praneeth Chakravarthula^{3†}

Hyemi Park²
Inki Kim^{2†}

Eunbyung Park^{1†}

¹ Yonsei University

² Sungkyunkwan University

³ University of North Carolina at Chapel Hill

Abstract

Metalens is an emerging optical system with an irreplaceable merit in that it can be manufactured in ultra-thin and compact sizes, which shows great promise in various applications. Despite its advantage in miniaturization, its practicality is constrained by spatially varying aberrations and distortions, which significantly degrade the image quality. Several previous arts have attempted to address different types of aberrations, yet most of them are mainly designed for the traditional bulky lens and ineffective to remedy harsh aberrations of the metalens. While there have existed aberration correction methods specifically for metalens, they still fall short of restoration quality. In this work, we propose a novel aberration correction framework for metalens-captured images, harnessing Vision Transformers (ViT) that have the potential to restore metalens images with non-uniform aberrations. Specifically, we devise a Multiple Adaptive Filters Guidance (MAFG), where multiple Wiener filters enrich the degraded input images with various noise-detail balances and a cross-attention module reweights the features considering the different degrees of aberrations. In addition, we introduce a Spatial and Transposed self-Attention Fusion (STAF) module, which aggregates features from spatial self-attention and transposed self-attention modules to further ameliorate aberration correction. We conduct extensive experiments, including correcting aberrated images and videos, and clean 3D reconstruction. The proposed method outperforms the previous arts by a significant margin. We further fabricate a metalens and verify the practicality of our method by restoring the images captured with the manufactured metalens. Code and pre-trained models are available at <https://benhenryl.github.io/Metalens-Transformer>.

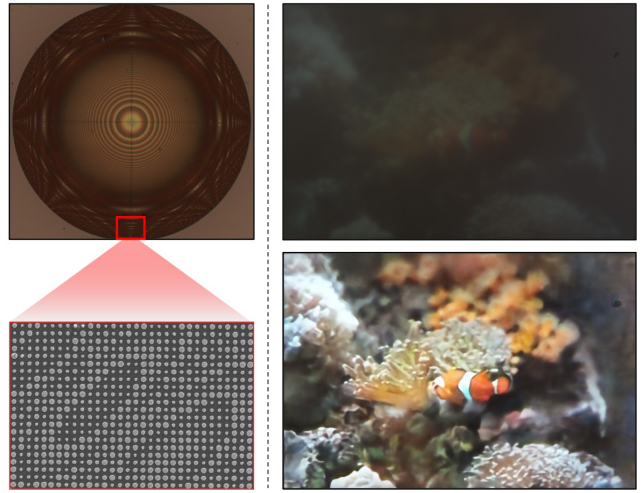


Figure 1. Left: The fabricated metalens. Right: An image captured with the manufactured metalens (top) and restored image with the proposed method (bottom).

1. Introduction

Metalens is an advanced optical device that leverages nanoscale engineering to manipulate light. Unlike traditional lenses relying on glass or plastic surfaces, the metalens harnesses a metasurface, a thin optical element consisting of nanostructures modulating optical properties such as phase and amplitude. It can be fabricated in ultra-thin and compact sizes, making it an ideal option for various domains, including the medical industries, consumer electronics, and augmented/virtual reality (AR/VR) [27, 39, 48, 50, 64, 74, 88, 96]. Despite its potential for miniaturization, existing metalenses have faced critical challenges, such as aberrations and distortions in the captured images, hampering their broad uses across diverse applications.

Aberrations in metalens occur due to practical constraints and the physical properties of lens materials. Wavelength-dependent nanostructures of the metasurface make different wavelengths of lights experience different

[†]Corresponding authors.

phase shifts, which results in them being focused at different points, leading to chromatic aberration. Furthermore, its spherical surface is susceptible to spherical aberrations where rays transmitting through the edges and center of the lens focus at different locations. Even worse, these aberrations are not uniform, rather varying across the image field, posing a more intricate problem of correcting them.

Several previous works [9, 21, 26] have attempted to correct these aberrations, primarily focusing on conventional camera lenses. While effective in some cases, these approaches fall short in addressing the unique challenges posed by metalens-induced aberrations. More recently, Tseng et al. [80] and Chakravarthula et al. [8] have proposed deep learning-based restoration methods for metalenses. Tseng et al. [80] adopted convolutional neural networks (CNNs) and Chakravarthula et al. [8] employed a diffusion model [32, 73] to correct distortions. While promising, they have yet to reach the desired restoration quality.

Besides the aberration corrections, extensive research has addressed other image degradations such as blur, noise, raindrops, haze, *etc.* Generative models [34, 42, 43, 62], CNNs [28, 45, 56, 59, 92, 94], or Vision Transformer (ViT) [12, 15, 51, 81, 93] have all been employed for image restoration, demonstrating strong performance. However, directly applying these methods to metalens-induced aberration correction is ineffective due to the aberration patterns of metalens that vary in response to different wavelengths, making them significantly more complex and challenging to correct using standard restoration techniques.

Among various frameworks, ViT-based approaches have a strong potential for metalens image restoration. ViT can effectively capture global context by leveraging the self-attention mechanism, allowing each pixel in an image to communicate with all others. This global receptive field is particularly advantageous for metalens restoration, where understanding the overall structure helps suppress noise and artifacts while preserving fine details. Moreover, self-attention modules enable dynamic weighting of features, encouraging them to learn spatially varying corrections, which is essential in metalens image restoration since the severity of aberration is different across the image. Despite these advantages, ViT-based methods remain largely unexplored for metalens restoration.

In this work, we propose a novel aberration correction Transformer specifically designed for metalens image restoration. First, we suggest a Multiple Adaptive Filters Guidance (MAFG) module, which leverages a set of Wiener filters [86] alongside a cross-attention mechanism to dynamically weight features for more effective aberration correction. MAFG offers two key advantages. First, it is well-suited for handling spatially varying aberrations. MAFG produces features that can consider different degrees of aberration by reweighting multiple features gen-

erated with different filters via cross-attention. Second, by employing filters with varying noise suppression parameters, MAFG enhances robustness against unknown aberration distributions, making it adaptable to a wide range of imaging conditions.

Furthermore, we propose a Spatial and Transposed self-Attention Fusion (STAF) module, which integrates both spatial and transposed self-attention to enhance feature aggregation while considering the distinct roles of the encoder and decoder. In STAF, spatial and transposed self-attention operate in parallel, with their features fused to guide the encoder in capturing global context and the decoder in refining fine details. We also encourage attention modules in the decoder to better capture intricate details, further improving restoration quality.

We conducted extensive experiments across various imaging scenarios to validate the effectiveness of the proposed method. On image dataset with spatially varying aberration, it demonstrated notable performance improvements. We further applied the proposed techniques to video restoration and 3D reconstruction tasks to confirm their superiority. Finally, we fabricated metalens using the open-source PSF of a metalens [80] and evaluated our method on the captured images. The corrected images demonstrated promising results, revealing new possibilities in metalens imaging. To sum up, our contributions are as follows:

- We propose a novel neural architecture for metalens image restoration, achieving state-of-the-art performance with a 6.45 dB improvement in PSNR over the baseline model.
- We devise a Multiple Adaptive Filters Guidance (MAFG) that employs several Wiener filters operating adaptively to various images to enrich features of representations.
- We design a Spatial and Transposed self-Attention Fusion (STAF) module that applies spatial and transposed self-attention well aligned with encoder-decoder architecture.
- We fabricated a metalens with the open-source PSF and constructed a metalens-captured image dataset.

2. Related Works

Metalens Recent advancements in nanofabrication have enabled the use of ultra-thin metasurfaces consisting of sub-wavelength scatterers that can independently adjust the amplitude, phase, and polarization of incident wavefronts, allowing for greater design flexibility [22, 25, 53, 58]. This flexibility has motivated research into applications such as flat meta-optics for imaging [1, 8, 11, 17, 25, 54, 80, 89], polarization control [3], and holography [98]. Notably, work by Tseng et al. [80] introduced a differentiable design for meta-optics achieving high image quality within a 0.5 mm aperture but with limitations in field performance beyond 40°. More recently, Chakravarthula et al. [8] introduced a metalens array design that enhances image quality across a

full broadband spectrum over a 100° field of view (FoV) without increasing the back focal length, potentially allowing for one-step fabrication directly on the camera sensor coverglass. However, existing meta-optics still face challenges with chromatic and geometric aberrations, limiting broadband imaging capabilities [2, 53, 83, 89]. Although dispersion engineering methods have mitigated some chromatic aberrations [4, 38, 63, 72, 82], they remain restricted to very small apertures [66]. In this work, we introduce a framework to compensate for aberrations and overcome the challenges faced by such meta-optics imaging cameras.

Image Restoration Models Image restoration aims to recover high-quality images from degraded observations. Traditionally, Wiener deconvolution [86] has been used to recover images by solving inverse problems. However, it often struggled with noise and complex degradations, limiting their real-world applications. Recently, deep learning-based methods have shown great success in image restoration tasks in a data-driven manner. Vision Transformer (ViT) [20], in particular, has achieved remarkable performances in various image restoration tasks, including denoising [10, 24, 49, 81, 85, 93], deblurring [41, 55, 79, 85, 93], and super resolution [13–15, 51, 57, 77], by exploiting self-attention, capturing global interactions effectively.

Restormer [93] stood out with its superior performance, introducing transposed self-attention mechanisms that apply self-attention across the channel of an image, enabling efficient processing of high-resolution images. While this approach enhances computational efficiency, it may limit the model’s ability to fully exploit spatial dependencies. To address this, X-Restormer [12] incorporated spatial self-attention mechanisms allowing for better capture of spatial relationships. In this work, building upon these advancements, we propose a novel architecture that further enhances restoration quality for metalens images.

Aberration Correction Models Optical aberration arises from imperfections in optical systems, with chromatic and spherical aberrations being frequently observed in the metalens imaging process. Chromatic aberration, where different wavelengths of light focus at different points, leads to color fringing, and spherical aberration occurs when the rays passing through the edges and center of the lens are focused at different points, resulting in blurriness. Extensive research has been conducted to correct these aberrations, and they can be broadly categorized into non-blind and blind aberration correction.

Non-blind approaches [16, 19, 29, 33, 36, 71, 97] require PSF calibration before training the models. Once the PSF is well calibrated, it can be consistently applied across various images, as optical aberrations are independent of the scene content in general [90, 91]. Especially, DWDN [19]

leveraged Wiener deconvolution [86] in the feature space for multi-scale refinement and Li et al. [47] proposed a PSF-aware network using patch-wise deconvolution with deep priors to cope with spatially varying aberrations.

Blind aberration correction approaches [21, 26, 68, 69, 78, 91] correct aberrations by estimating aberration kernels without any prior PSF information. Eboli et al. [21] adopted a small CNN for color correction, and Gong et al. [26] utilized the physical properties of lenses to improve image quality. These blind methods can be applied generally without demanding preprocess (*e.g.*, PSF calibration), but restoration quality may suffer due to uncertainties in accurately estimating the PSF.

Several aberration correction models have been specifically designed for metalens imaging [8, 80]. Tseng et al. [80] employed CNNs and Wiener filters for restoration but faced challenges in preserving fine image details. This limitation may arise from the restricted receptive field of CNNs. Chakravarthula et al. [8] introduced diffusion models [32, 73] with Wiener filters to manage aberrations, yet it can generate unrealistic details due to the stochasticity of the diffusion, compromising the overall image quality.

Aberration correction presents unique challenges in metalens imaging, yet the potential of Vision Transformers (ViT) has not been fully explored for this task. In this paper, we propose a novel approach that leverages ViT, developing new architectural modules and adapting its attention mechanisms to effectively handle the complex aberration patterns in metalens imaging.

3. Methods

Fig. 2 depicts the overall architecture of the proposed method. It consists of Vision Transformer (ViT) as a backbone network for restoration (Sec. 3.2), Multiple Adaptive Filters Guidance (MAFG) (Sec. 3.3), and Spatial and Transposed self-Attention Fusion (STAF) blocks (Sec. 3.4).

3.1. Preliminary

Metalens Imaging An imaging formulation using a spatially varying point spread function (PSF) can be written in patch-level imaging as follows,

$$I_{abr}[h, w] = I_c[h, w] * PSF[h, w] + n[h, w], \quad (1)$$

where $[\cdot, \cdot]$ is an indexing operator, $*$ denotes the convolution operator, $h \in \{1, 2, \dots, H\}$ and $w \in \{1, 2, \dots, W\}$ are the indices of $H \times W$ image and PSF patches. $I_{abr}[h, w]$ is the observed image, which can be represented as the convolution of an object $I_c[h, w]$ with a corresponding PSF at patch $[h, w]$. Then the noise $n[h, w]$, such as shutter and natural noise, is added to generate the captured image I_{abr} . The PSF of metalens varies significantly with wavelength because different colors focus at different distances from

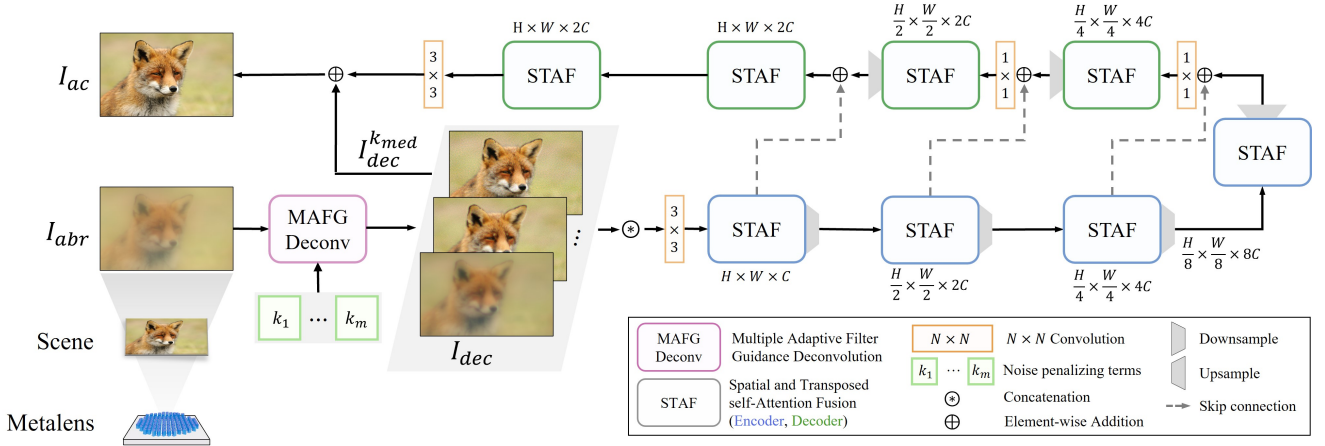


Figure 2. The overview of our method. It comprises Multiple Adaptive Filters Guidance (MAFG) which produces different representations with various noise-detail balances, and a Spatial and Transposed self-Attention Fusion (STAF) module that aggregates features differently in encoder and decoder.

the metalens. This produces color fringing and a low contrast in the captured image. Such optical degradations vary gradually across the field of view, implying the distortions are similar within a small neighborhood; hence, the imaging can be formulated at a patch level.

3.2. Vision Transformer for Metalens Images

As discussed, various ViT-based approaches [14, 15, 51, 55, 77, 81, 85, 93] have been developed for restoring images captured by traditional cameras. While ViT has not been fully explored for metalens image restoration, it inherently has promising capabilities to handle the severe aberrations present in metalens images. First, ViT can adaptively adjust its attention weight to focus on different areas of the image, making it particularly suited for handling the spatially varying aberrations of metalens imaging. Furthermore, chromatic aberrations of metalens differ across different wavelengths of light, causing each image channel to be affected differently. ViT’s multi-head attention mechanism allows it to model these channel-specific discrepancies, processing each channel effectively. Lastly, metalens-induced aberrations can degrade the images at various scales, affecting both high-frequency details (*e.g.*, color fringes at sharp edges) and low-frequency components (*e.g.*, gradual intensity shifts). ViT’s ability to capture multi-scale features enhances its capacity to correct different types of distortions.

Such capabilities motivated us to adopt ViT for metalens image restoration. Nevertheless, applying ViT directly to metalens image restoration is ineffective, as metalenses introduce more complex aberrations and distortions than conventional lenses, demanding a more specialized solution. Therefore, we employ ViT as the backbone network and incorporate novel aberration-correcting modules to better align ViT with the specific challenges of metalens imaging.

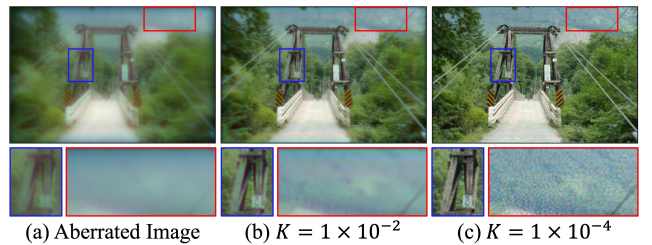


Figure 3. A comparison of the Wiener deconvolved images with different noise-penalization terms K . High K produces smooth representation (b), while smaller K results in a more textured but noisy representation (c).

3.3. Multiple Adaptive Filters Guidance

Before feeding the aberrated images to the restoration network, we deconvolve the image first with multiple Wiener filters [86]. Wiener filter is a linear filter that has been used to reduce noise in signals, in the context of image processing and restoration [18, 19, 31, 67, 97, 99]. It can balance noise suppression and detail preservation by exploiting the signal-to-noise ratio (SNR), which makes it particularly effective in image restoration tasks. Given a PSF, the Wiener filter in the frequency domain, W , is defined as follows,

$$W[u, v] = \frac{H^*[u, v]}{|H[u, v]|^2 + K}, \quad (2)$$

where u and v are horizontal and vertical spatial frequency respectively, H is a fourier transformed PSF, H^* is a complex conjugation of H , and K is an inverse of SNR. Note that each color channel has a different PSF, but we do not explicitly denote the channel for brevity, *e.g.* H_c or W_c .

As shown in Fig. 3, K plays a pivotal role in penalizing the noise; a greater K leads to a smoother representation, whereas a smaller K can preserve more high-frequency details, albeit with the increased noise. Inspired by this, we

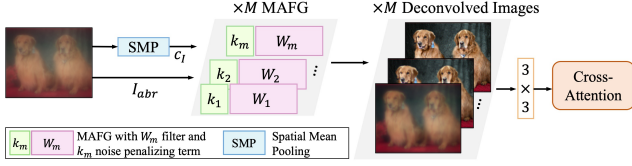


Figure 4. The process of Multiple Adaptive Filters Guidance (MAFG). It produces M different representations from the input images using M different Wiener filters and applies cross-attention to reweight them.

propose to use multiple Wiener filters to guide aberration correction with several distinct representations. It is not feasible to obtain an optimal Wiener filter with accurate SNR as noise distribution is unknown in the real world. Such design can approximate the ideal filter by employing M filters with different K in a wide range.

Furthermore, we extend multiple Wiener filters to Multiple Adaptive Filters Guidance (MAFG), illustrated in Fig. 4, which determines K adaptively considering the image intensity. Image with higher intensity tends to have better signal quality, so brighter channels often experience less noise [23]. Thus, we penalize noise less and capture more information for bright images by adjusting K with the image intensity. Also, we treat each channel differently to avoid suppressing high-SNR details unnecessarily, since metalens exhibit wavelength-dependent aberrations where each color channel suffers differently due to the different chromatic responses. Based on this observation, we slightly modify Eq. (2) for MAFG as follows:

$$W_m[u, v] = \frac{H^*[u, v]}{|H[u, v]|^2 + k_m \cdot (1 - c_I)}, \quad (3)$$

where $m \in \{1, \dots, M\}$ is the index of M different filters, $c_I \in \mathbb{R}$ is the average intensity of each color channel, and $k_m \in \mathbb{R}$ is a hyperparameter for scaling c_I . The proposed MAFG is adaptive to the input images, which allows flexible responses to the various images.

We obtain M different deconvolved images $\{I_{dec}^m\}_{m=1}^M$ using MAFG with the following equation:

$$I_{dec}^m[x, y] = \text{ifft}(W_m \odot \text{fft}(I_{abr}))[x, y], \quad (4)$$

where fft and ifft are Fast Fourier Transform (FFT) and the inverse FFT [7], respectively. ‘ \odot ’ is the Hadamard product, x and y are pixel coordinates.

Then, they are processed by a cross-attention block, where the query is $I_{dec}^{k_{med}}$, the deconvolved image with a median of k_m , which is a compromise between noise suppression and detail preservation. Cross-attention can reweight the features, which it can attend more to the filter outputs with high k_m (severe aberration, red boxes in Fig. 3) or it can favor the filter outputs with low k_m (mildly aberrated parts, blue boxes in Fig. 3), resulting in spatially

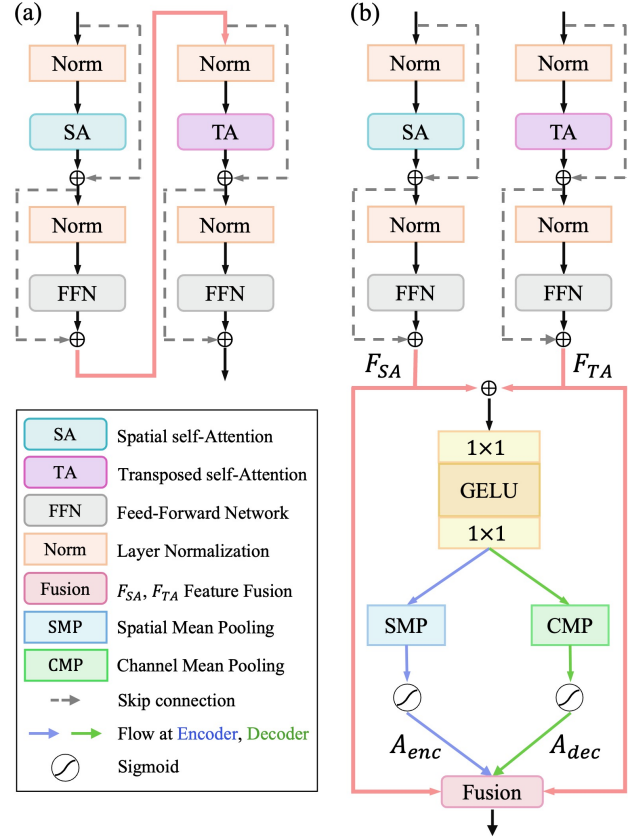


Figure 5. Comparison on applying SA and TA. (a). Previous works that apply SA and TA alternatively. (b). Proposed Spatial and Transposed self-Attention Fusion (STAF). It implements SA and TA in parallel and fuses features with different weights in the encoder and decoder.

adaptive correction. This is especially important for metalens images, where aberration occurs non-uniformly. The reweighted feature is then fed to the restoration network.

3.4. Spatial and Transposed Self-Attention Fusion

As aforementioned, a variety of previous studies adopted spatial self-attention (SA) [14, 51], transposed self-attention (TA) [93], or both [12, 15, 81] for image restoration. Leveraging both SA and TA, by alternatively applying them as depicted in Fig. 5 (a), can encode spatial context effectively.

Nevertheless, there remains room for improvement, as existing methods apply SA and TA uniformly across both encoder and decoder stages despite their distinct objectives. The encoder primarily focuses on capturing a global context, emphasizing the overall structure and relationships within the images, which helps identify patterns and features. In contrast, the decoder mainly aims to recover local details and textures essential for high-fidelity restoration.

Therefore, we propose a Spatial and Transposed self-Attention Fusion (STAF) module which implements SA and TA separately, not alternatively, and fuses SA and TA fea-

tures with different weights in the encoder and decoder, as depicted in Fig. 5 (b). In detail, the outcome of SA and TA (denoted as $F_{SA}, F_{TA} \in \mathbb{R}^{H \times W \times C}$, respectively and H, W, C are height, width, and channel of the input feature) are concatenated along channel dimension to obtain concatenated feature $F \in \mathbb{R}^{H \times W \times 2C}$. F is then fed to a small CNN, consisting of two 1×1 convolution layers with GELU activation [30], to mix features and halve channel dimension to C , and produce $A \in \mathbb{R}^{H \times W \times C}$, which is then treated differently in encoder and decoder. At the encoder side, we employ average pooling to A on spatial dimensions to efficiently reduce resolution while preserving crucial feature representations and obtain weight matrix $A_{enc} \in \mathbb{R}^{1 \times 1 \times C}$. On the other hand, A is averaged along the channel dimension to selectively emphasize the relevant feature maps and produce a weight matrix $A_{dec} \in \mathbb{R}^{H \times W \times 1}$ for the decoder. This allows the decoder to prioritize different spatial areas. In a nutshell, A_{enc} and A_{dec} can be computed as follows:

$$\begin{aligned} F &= \text{Concat}(F_{SA}, F_{TA}), \\ A &= \text{Conv}(\text{GELU}(\text{Conv}(F))), \\ A_{enc} &= \sigma(\text{AVGPool}_{H,W}(A)), \\ A_{dec} &= \sigma(\text{AVGPool}_C(A)), \end{aligned} \quad (5)$$

where σ is the sigmoid activation, and $\text{AVGPool}_{H,W}$ and AVGPool_C are average pooling along the height and width dimension and channel dimension, respectively. A_{enc} and A_{dec} are then used to compute the final feature of each block where F_{SA} and F_{TA} are mixed properly for the encoder and decoder with the equations:

$$\begin{aligned} F_{enc} &= F_{SA} \odot A_{enc} + F_{TA} \odot (1 - A_{enc}), \\ F_{dec} &= F_{SA} \odot A_{dec} + F_{TA} \odot (1 - A_{dec}), \end{aligned} \quad (6)$$

where \odot denotes the Hadamard product, and the index for each layer is omitted for brevity.

To further compensate for fine detail losses due to the harsh aberration, we enforce the queries of both attention modules in the decoder to focus more on high-frequency information, inspired by ESRT [57] that estimates high-frequency information of the feature using average pooling. In particular, we adopt this enhanced query Q_{dec}^b in every other block of each decoder layer, as follows:

$$Q_{dec}^b = \begin{cases} Q_{dec}^b, & \text{if } b = 2n \\ Q_{dec}^b - \text{AVGPool}(Q_{dec}^b), & \text{if } b = 2n + 1, \end{cases} \quad (7)$$

where b is a block index, $n \in \mathbb{Z}$, Q_{dec}^b is an original query from the previous block, and the index of the layer is again omitted for brevity. This enhanced query is used in the SA and TA blocks of the decoder to compute F_{dec} . Finally, the residual obtained after forwarding all STAF blocks is added to the $I_{dec}^{k_{med}}$, to get the corrected image I_{ac} .



Figure 6. Generated point spread functions (PSFs) and an image with spatially varying aberration derived from them.

4. Experiments

4.1. Experimental Settings

We divided FOV into 9×9 grid and generated 81 PSFs using metalens phase profile from Tseng et al. [80] to represent spatially varying aberration of metalens imaging as shown in Fig. 6, following Eq. (1). We set the number of filters $M = 13$ and selected 13 logarithmically spaced values in the range $[1e - 5, 1e - 2]$ for noise penalizing scalars k_m .

We conducted experiments across various tasks: image aberration correction (Sec. 3.4), restoring images captured with the fabricated metalens (Sec. 4.3), video aberration correction (Sec. 4.4), and 3D reconstruction with aberrated images (Sec. 4.5). Analysis on the method, detailed experimental settings, and more experimental results are described in the supplementary material.

4.2. Image Aberration Correction

We adopted Open Image V7 [6, 44] dataset with spatially varying aberration for image aberration correction task, and sampled 120K and 1K images for training and validation, respectively. We constructed two different types of test sets, one with spatially varying aberrations from 81 different PSFs, and the other with spatially invariant aberration, where we selected 5 PSFs at different field angles (0° , 5° , 10° , 15° , and 20°), each corresponding to a distinct uniform aberration.

Tab. 1, Fig. 7 and Fig. 8 provide the results on the spatially varying and invariant aberration test sets¹, where *Restormer+SWF* is a *non-blindly* trained Restormer using a single Wiener filter. As shown in input images in Fig. 8, an image degraded by the PSF at a large field angle suffers more from aberration, which corresponds to the outer parts of the image with spatially varying aberration in Fig. 7.

Spatially Varying Aberration Tseng et al. [80] leverages the PSF to address aberrations but fails to preserve fine details and contrast, highlighting the limitations of CNNs for metalens imaging. Restormer [93] demonstrates the capability of ViTs in metalens imaging by restoring the mildly aberrated region (blue box in Fig. 7) without PSF guidance. However, it fails to correct pronounced aberrations in off-axis areas (red box in Fig. 7). Non-blindly training

¹The codes and pre-trained weights for Chakravarthula et al. [8] were not publicly available, so we could only compare with Tseng et al. [80].

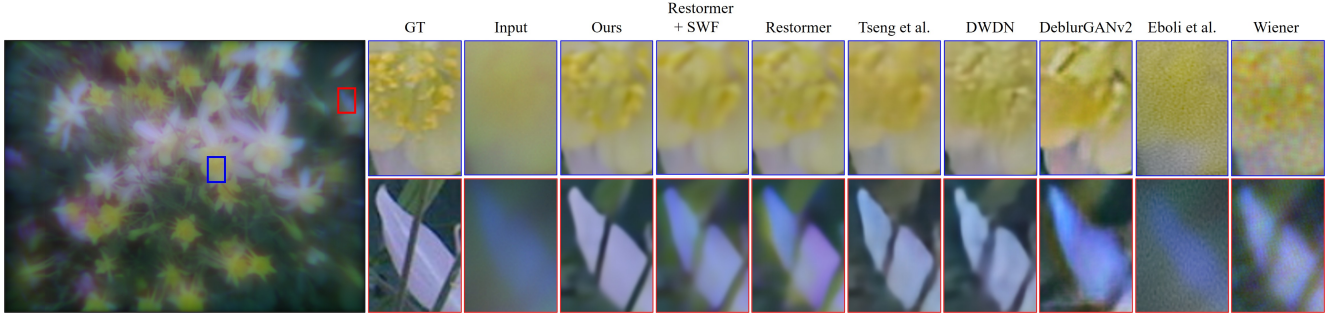


Figure 7. Qualitative results on the Open Image V7 [6, 44] dataset with spatially varying aberration.

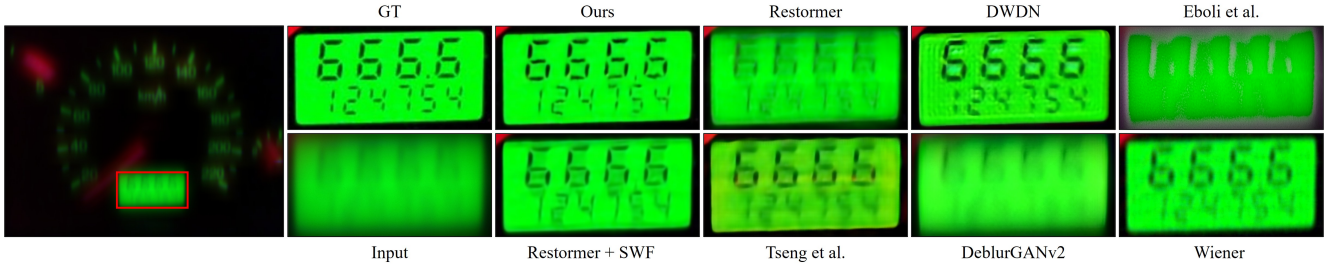


Figure 8. Qualitative results on the Open Image V7 [6, 44] dataset with the uniform aberration at field angle 20° .

Method	Non-uniform aberration			Uniform aberration at $\theta = 0^\circ$			Uniform aberration at $\theta = 20^\circ$		
	PSNR \uparrow	SSIM \uparrow	LPIPS \downarrow	PSNR \uparrow	SSIM \uparrow	LPIPS \downarrow	PSNR \uparrow	SSIM \uparrow	LPIPS \downarrow
Wiener deconvolution [86]	25.54	0.5743	0.5228	27.06	0.6561	0.4458	26.05	0.6332	0.5030
Eboli et al. [21]	15.19	0.3784	0.8270	20.73	0.5359	0.6488	18.55	0.4480	0.7973
DeblurGANv2 [43]	24.08	0.6863	0.3233	25.27	0.7338	0.3032	21.79	0.6048	0.4810
DWDN [19]	26.40	0.7656	0.2854	29.38	0.8318	0.2459	25.68	0.7282	0.3267
Tseng et al. [80]	28.66	0.8045	0.2949	29.88	0.8373	0.2507	28.09	0.7841	0.3117
Restormer [93]	27.84	0.8091	0.2753	31.09	0.8827	0.1804	28.53	0.8020	0.2871
Restormer [93] + SWF	29.87	0.8289	0.2812	33.58	0.8804	0.2003	28.95	0.7908	0.3262
Ours	34.29	0.8760	0.2052	35.06	0.8961	0.1763	32.32	0.8409	0.2542

Table 1. Quantitative results Open Image V7 [6, 44] dataset with spatially varying and invariant aberration, where θ denotes a field angle.

Restormer with a single Wiener filter still struggles with recovering fine details. In contrast, our approach effectively corrects aberrations across both on- and off-axis regions, achieving state-of-the-art results with a noticeable margin.

Spatially Invariant Aberration Tseng et al. [80] models spatially varying aberration by utilizing multiple patches with different degrees of aberration. However, since each patch assumes a single type of aberration (i.e., uniform aberration), seam-like artifacts may emerge when applied to the image where diverse aberrations coexist within a single frame, which is common in real scenarios. To ensure a fair comparison, we further conducted experiments under uniform aberration conditions. As demonstrated in Tab. 1 and Fig. 8, our method effectively models spatially varying aberrations, achieving robust performance even in cases where severe aberrations (at field angle 20°) appear uniformly, outperforming Tseng et al. [80].

Method	PSNR \uparrow	SSIM \uparrow	LPIPS \downarrow
VRT [52]	23.23	0.6906	0.3921
VRT w/ Ours	28.89	0.8602	0.2102

Table 2. Quantitative results on the aberrated DVD dataset [75].

4.3. Images from the Fabricated Metalens

We fabricated a metalens with the PSF from Tseng et al. [80] as shown in Fig. 9 (Left) and captured images to construct a dataset. It consists of 220 images, where 200 images are involved in fine-tuning the pre-trained model from Sec. 3.4, and 20 images are kept for validation. Since ViT requires a larger volume of training data, large-scale dataset construction is inevitable, which is labor-intensive. Instead, we trained a model with numerous data simulated with the same phase profile of the manufactured metalens, and then fine-tuned it with the small set of captured images, easing the cost of collecting data. We fine-tuned our model, Restormer [93] and non-blind Restormer under the same experimental setting. As shown in Fig. 9, both Restormer



Figure 9. Qualitative results on the images captured with our fabricated metalens.

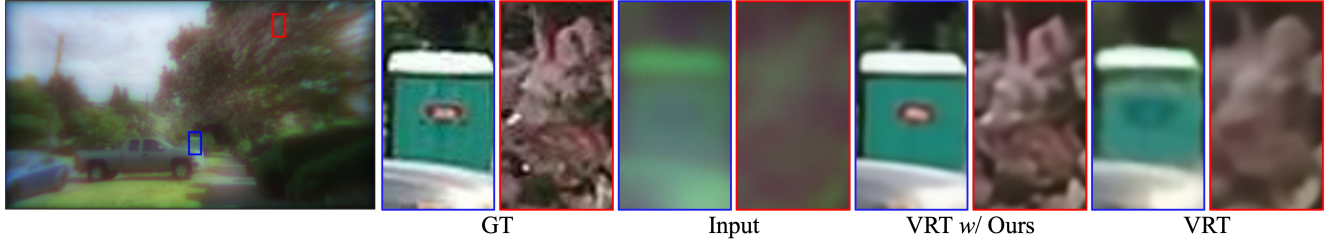


Figure 10. Qualitative results on the aberrated DVD [75] dataset.

Method	LLFF [60]			Tanks&Temples [40]		
	PSNR \uparrow	SSIM \uparrow	LPIPS \downarrow	PSNR \uparrow	SSIM \uparrow	LPIPS \downarrow
3D-GS [37]	17.43	0.4083	0.7428	16.81	0.3875	0.7263
3D-GS w/ Ours	25.29	0.7513	0.2138	23.17	0.6852	0.2639
3D-GS + Ours	25.49	0.7548	0.2149	23.30	0.6905	0.2632

Table 3. Quantitative results on the LLFF [60] and Tanks&Temples [40] dataset with spatially varying aberration.

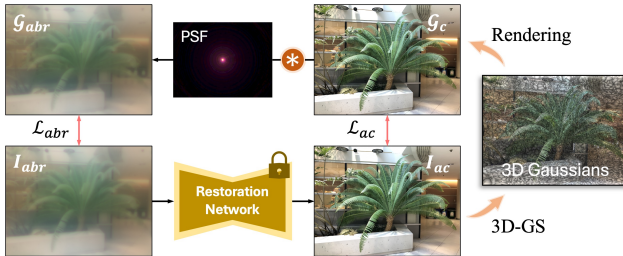


Figure 11. Training pipeline for 3D-GS using the proposed ViT.

and non-blind Restormer produce images in low contrast while the proposed method yields images with better contrast, leading to more visually appealing quality.

4.4. Video Aberration Correction

In this section, we assessed our method for the video aberration correction task. We employed VRT [52] as a baseline video restoration model and trained it on the DVD [75] dataset with spatially varying aberration. We trained VRT with the output of pre-trained model (VRT w/ Ours) from Sec. 3.4. Tab. 2 and Fig. 10 show that VRT struggled with correcting the aberration of the input video while VRT w/ Ours could enjoy both temporal consistency and clean representations.

4.5. 3D Reconstruction with Aberrated Images

We further extended our method to clean 3D reconstruction, training 3D Gaussian Splatting (3D-GS) [37] with the sets of multi-view aberrated images. We embedded our method



Figure 12. Qualitative results on the aberrated LLFF [40] (Top) and Tanks&Temples [40] (Bottom) dataset.

into 3D-GS training pipeline as delineated in Fig. 11. Specifically, we simulated aberration during 3D-GS training using Eq. (1) to constrain 3D-GS learning clean representations. The output (I_{ac}) of our pre-trained ViT, which is frozen during 3D-GS training, is involved in supervising the rendered image (G_c) with a loss $\mathcal{L}_{ac} = \mathcal{L}_{GS}(G_c, I_{ac})$ where \mathcal{L}_{GS} is a reconstruction loss function defined in 3D-GS. The aberration-simulated image G_{abr} is used to compute a loss $\mathcal{L}_{abr} = \mathcal{L}_{GS}(G_{abr}, I_{abr})$, with the training image I_{abr} . We use a sum of these losses, $\mathcal{L}_{train} = \mathcal{L}_{abr} + \lambda\mathcal{L}_{ac}$, to guide 3D-GS learning clean features from the aberrated images, where λ is a hyperparameter.

Tab. 3 and provide the results on the 3D reconstruction task, evaluated on LLFF [60] and Tanks&Temples [40] dataset with spatially variant aberration where we used only *Truck* and *Train* scenes in Tanks&Temples dataset for evaluation, following the experimental setting in 3D-GS. While 3D-GS fails to render clean images, the proposed pipeline that combines 3D-GS and our image restoration model (3D-GS + Ours) shows sound reconstruction performance, even outperforming 3D-GS optimized with the restored output I_{ac} from the proposed image correction model (3D-GS w/ Ours). This is because 3D-GS + Ours can learn

clean representation via \mathcal{L}_{ac} and multi-view consistency with \mathcal{L}_{abr} simultaneously, resulting in better reconstruction quality. Fig. 12 shows qualitative results, where the proposed method can produce clean images in novel views, while vanilla 3D-GS still suffers from severe aberration.

5. Conclusion

We present an aberration correcting transformer tailored for metalens imaging. We harness a Vision Transformer (ViT) that has not been fully explored in metalens imaging. We devise Multiple Adaptive Filters Guidance (MAFG) that can better model spatially varying aberration of metalens images and Spatial and Transposed self-Attention Fusion (STAF) which exploits features from SA and TA considering the roles of the encoder and decoder. The comprehensive experiments show the proposed method achieving state-of-the-art performance across diverse tasks. We also fabricate a metalens and effectively restore the captured images, proving the practicality of the proposed method.

References

- [1] Francesco Aieta, Patrice Genevet, Mikhail A. Kats, Nanfang Yu, Romain Blanchard, Zeno Gaburro, and Federico Capasso. Aberration-free ultrathin flat lenses and axicons at telecom wavelengths based on plasmonic metasurfaces. *Nano Letters*, 12(9):4932–4936, 2012. 2
- [2] Francesco Aieta, Mikhail A. Kats, Patrice Genevet, and Federico Capasso. Multiwavelength achromatic metasurfaces by dispersive phase compensation. *Science*, 347:1342–1345, 2015. 3
- [3] Amir Arbabi, Yu Horie, Mahmood Bagheri, and Andrei Faraon. Dielectric metasurfaces for complete control of phase and polarization with subwavelength spatial resolution and high transmission. *Nature Nanotechnology*, 10:937–943, 2015. 2
- [4] Ehsan Arbabi, Amir Arbabi, Seyedeh Mahsa Kamali, Yu Horie, and Andrei Faraon. Controlling the sign of chromatic dispersion in diffractive optics with dielectric metasurfaces. *Optica*, 4(6):625–632, 2017. 3
- [5] Jonathan T Barron, Ben Mildenhall, Dor Verbin, Pratul P Srinivasan, and Peter Hedman. Mip-nerf 360: Unbounded anti-aliased neural radiance fields. In *Proceedings of the IEEE/CVF conference on computer vision and pattern recognition*, pages 5470–5479, 2022. 16, 22
- [6] Rodrigo Benenson and Vittorio Ferrari. From colouring-in to pointillism: revisiting semantic segmentation supervision. *arXiv preprint arXiv:2210.14142*, 2022. 6, 7, 15, 16, 17, 18
- [7] EO Brigham. The fast fourier transform and its applications, 1988. 5
- [8] Praneeth Chakravarthula, Jipeng Sun, Xiao Li, Chenyang Lei, Gene Chou, Mario Bijelic, Johannes Froesch, Arka Majumdar, and Felix Heide. Thin on-sensor nanophotonic array cameras. *ACM Transactions on Graphics (TOG)*, 42(6):1–18, 2023. 2, 3, 6
- [9] Joonyoung Chang, Hee Kang, and Moon Gi Kang. Correction of axial and lateral chromatic aberration with false color filtering. *IEEE Transactions on Image Processing*, 22(3): 1186–1198, 2012. 2
- [10] Hanqing Chen, Yunhe Wang, Tianyu Guo, Chang Xu, Yiping Deng, Zhenhua Liu, Siwei Ma, Chunjing Xu, Chao Xu, and Wen Gao. Pre-trained image processing transformer. In *CVPR*, 2021. 3
- [11] Ji Chen, Xin Ye, Shenglun Gao, Yuxin Chen, Yunwei Zhao, Chunyu Huang, Kai Qiu, Shining Zhu, and Tao Li. Planar wide-angle-imaging camera enabled by metalens array. *Optica*, 9(4):431–437, 2022. 2
- [12] Xiangyu Chen, Zheyuan Li, Yuandong Pu, Yihao Liu, Jiantao Zhou, Yu Qiao, and Chao Dong. A comparative study of image restoration networks for general backbone network design. *arXiv preprint arXiv:2310.11881*, 2023. 2, 3, 5, 14, 15
- [13] Xiangyu Chen, Xintao Wang, Jiantao Zhou, Yu Qiao, and Chao Dong. Activating more pixels in image super-resolution transformer. In *Proceedings of the IEEE/CVF Conference on Computer Vision and Pattern Recognition (CVPR)*, pages 22367–22377, 2023. 3
- [14] Xiangyu Chen, Xintao Wang, Jiantao Zhou, Yu Qiao, and Chao Dong. Activating more pixels in image super-resolution transformer. In *Proceedings of the IEEE/CVF conference on computer vision and pattern recognition*, pages 22367–22377, 2023. 4, 5, 15
- [15] Zheng Chen, Yulun Zhang, Jinjin Gu, Linghe Kong, Xiaokang Yang, and Fisher Yu. Dual aggregation transformer for image super-resolution. In *Proceedings of the IEEE/CVF international conference on computer vision*, pages 12312–12321, 2023. 2, 3, 4, 5, 14
- [16] Sunghyun Cho, Jue Wang, and Seungyong Lee. Handling outliers in non-blind image deconvolution. In *2011 International Conference on Computer Vision*, pages 495–502. IEEE, 2011. 3
- [17] Shane Colburn, Alan Zhan, and Arka Majumdar. Metasurface optics for full-color computational imaging. *Science Advances*, 4:eaar2114, 2018. 2
- [18] Jiangxin Dong, Stefan Roth, and Bernt Schiele. Deep wiener deconvolution: Wiener meets deep learning for image deblurring. *Advances in Neural Information Processing Systems*, 33:1048–1059, 2020. 4
- [19] Jiangxin Dong, Stefan Roth, and Bernt Schiele. Dwdn: Deep wiener deconvolution network for non-blind image deblurring. *IEEE Transactions on Pattern Analysis and Machine Intelligence*, 44(12):9960–9976, 2021. 3, 4, 7, 16
- [20] Alexey Dosovitskiy. An image is worth 16x16 words: Transformers for image recognition at scale. *arXiv preprint arXiv:2010.11929*, 2020. 3
- [21] Thomas Eboli, Jean-Michel Morel, and Gabriele Facciolo. Fast two-step blind optical aberration correction. In *European Conference on Computer Vision*, pages 693–708. Springer, 2022. 2, 3, 7, 16
- [22] Jacob Engelberg and Uriel Levy. The advantages of metalenses over diffractive lenses. *Nature Communications*, 11: 1991, 2020. 2

- [23] Baris I Erkmen and Jeffrey H Shapiro. Signal-to-noise ratio of gaussian-state ghost imaging. *Physical Review A—Atomic, Molecular, and Optical Physics*, 79(2):023833, 2009. 5
- [24] Chi-Mao Fan, Tsung-Jung Liu, and Kuan-Hsien Liu. Sunet: swin transformer unet for image denoising. In *2022 IEEE International Symposium on Circuits and Systems (ISCAS)*, pages 2333–2337. IEEE, 2022. 3
- [25] Johannes E Fröch, Praneeth K Chakravarthula, Jipeng Sun, Ethan Tseng, Shane Colburn, Alan Zhan, Forrest Miller, Anna Wirth-Singh, Quentin AA Tanguy, Zheyi Han, et al. Beating bandwidth limits for large aperture broadband nano-optics. *arXiv preprint arXiv:2402.06824*, 2024. 2
- [26] Jin Gong, Runzhao Yang, Weihang Zhang, Jinli Suo, and Qionghai Dai. A physics-informed low-rank deep neural network for blind and universal lens aberration correction. In *Proceedings of the IEEE/CVF Conference on Computer Vision and Pattern Recognition*, pages 24861–24870, 2024. 2, 3
- [27] Tian Gu, Hyun Jung Kim, Clara Rivero-Baleine, and Juejun Hu. Reconfigurable metasurfaces towards commercial success. *Nature Photonics*, 17(1):48–58, 2023. 1
- [28] Jingwen He, Chao Dong, and Yu Qiao. Modulating image restoration with continual levels via adaptive feature modification layers. In *The IEEE Conference on Computer Vision and Pattern Recognition (CVPR)*, 2019. 2
- [29] Felix Heide, Mushfiqur Rouf, Matthias B Hullin, Bjorn Labitzke, Wolfgang Heidrich, and Andreas Kolb. High-quality computational imaging through simple lenses. *ACM Transactions on Graphics (ToG)*, 32(5):1–14, 2013. 3
- [30] Dan Hendrycks and Kevin Gimpel. Gaussian error linear units (gelus). *arXiv preprint arXiv:1606.08415*, 2016. 6
- [31] AD Hiller and Roland T Chin. Iterative wiener filters for image restoration. In *International Conference on Acoustics, Speech, and Signal Processing*, pages 1901–1904. IEEE, 1990. 4
- [32] Jonathan Ho, Ajay Jain, and Pieter Abbeel. Denoising diffusion probabilistic models. *Advances in neural information processing systems*, 33:6840–6851, 2020. 2, 3
- [33] Neel Joshi, Richard Szeliski, and David J Kriegman. Psf estimation using sharp edge prediction. In *2008 IEEE Conference on Computer Vision and Pattern Recognition*, pages 1–8. IEEE, 2008. 3
- [34] Bahjat Kawar, Michael Elad, Stefano Ermon, and Jiaming Song. Denoising diffusion restoration models. *Advances in Neural Information Processing Systems*, 35:23593–23606, 2022. 2
- [35] Junjie Ke, Qifei Wang, Yilin Wang, Peyman Milanfar, and Feng Yang. Musiq: Multi-scale image quality transformer. In *Proceedings of the IEEE/CVF international conference on computer vision*, pages 5148–5157, 2021. 15
- [36] Eric Kee, Sylvain Paris, Simon Chen, and Jue Wang. Modeling and removing spatially-varying optical blur. In *2011 IEEE international conference on computational photography (ICCP)*, pages 1–8. IEEE, 2011. 3
- [37] Bernhard Kerbl, Georgios Kopanas, Thomas Leimkühler, and George Drettakis. 3d gaussian splatting for real-time radiance field rendering. *ACM Trans. Graph.*, 42(4):139–1, 2023. 8, 16
- [38] Mohammadreza Khorasaninejad, Zhujun Shi, Alexander Y Zhu, Wei-Ting Chen, Vyshakh Sanjeev, Aun Zaidi, and Federico Capasso. Achromatic metalens over 60 nm bandwidth in the visible and metalens with reverse chromatic dispersion. *Nano Letters*, 17(3):1819–1824, 2017. 3
- [39] Sun-Je Kim, Changhyun Kim, Youngjin Kim, Jinsoo Jeong, Seokho Choi, Woojun Han, Jaisoon Kim, and Byoung-ho Lee. Dielectric metalens: properties and three-dimensional imaging applications. *Sensors*, 21(13):4584, 2021. 1
- [40] Arno Knapitsch, Jaesik Park, Qian-Yi Zhou, and Vladlen Koltun. Tanks and temples: Benchmarking large-scale scene reconstruction. *ACM Transactions on Graphics (ToG)*, 36(4):1–13, 2017. 8, 16, 21
- [41] Lingshun Kong, Jiangxin Dong, Mingqiang Li, Jianjun Ge, and Jinshan Pan. Efficient frequency domain-based transformers for high-quality image deblurring, 2022. 3
- [42] Orest Kupyn, Volodymyr Budzan, Mykola Mykhailych, Dmytro Mishkin, and Jiří Matas. Deblurgan: Blind motion deblurring using conditional adversarial networks. In *Proceedings of the IEEE conference on computer vision and pattern recognition*, pages 8183–8192, 2018. 2
- [43] Orest Kupyn, Tetiana Martyniuk, Junru Wu, and Zhangyang Wang. Deblurgan-v2: Deblurring (orders-of-magnitude) faster and better. In *Proceedings of the IEEE/CVF international conference on computer vision*, pages 8878–8887, 2019. 2, 7, 16
- [44] Alina Kuznetsova, Hassan Rom, Neil Alldrin, Jasper Uijlings, Ivan Krasin, Jordi Pont-Tuset, Shahab Kamali, Stefan Popov, Matteo Mallocci, Alexander Kolesnikov, et al. The open images dataset v4: Unified image classification, object detection, and visual relationship detection at scale. *International journal of computer vision*, 128(7):1956–1981, 2020. 6, 7, 15, 16, 17, 18
- [45] Bruno Lecouat, Jean Ponce, and Julien Mairal. Fully trainable and interpretable non-local sparse models for image restoration. *Proc. European Conference on Computer Vision (ECCV)*, 2020. 2
- [46] Byeonghyeon Lee, Howoong Lee, Xiangyu Sun, Usman Ali, and Eunbyung Park. Deblurring 3d gaussian splatting. *arXiv preprint arXiv:2401.00834*, 2024. 16
- [47] Xiu Li, Jinli Suo, Weihang Zhang, Xin Yuan, and Qionghai Dai. Universal and flexible optical aberration correction using deep-prior based deconvolution. In *Proceedings of the IEEE/CVF International Conference on Computer Vision*, pages 2613–2621, 2021. 3
- [48] Yan Li, Shuyi Chen, Haowen Liang, Xiuying Ren, Lingcong Luo, Yuye Ling, Shuxin Liu, Yikai Su, and Shin-Tson Wu. Ultracompact multifunctional metalens visor for augmented reality displays. *PhotonIX*, 3(1):29, 2022. 1
- [49] Yawei Li, Yuchen Fan, Xiaoyu Xiang, Denis Demandolx, Rakesh Ranjan, Radu Timofte, and Luc Van Gool. Efficient and explicit modelling of image hierarchies for image restoration. In *Proceedings of the IEEE/CVF Conference on Computer Vision and Pattern Recognition*, pages 18278–18289, 2023. 3

- [50] Zhaoyi Li, Peng Lin, Yao-Wei Huang, Joon-Suh Park, Wei Ting Chen, Zhujun Shi, Cheng-Wei Qiu, Ji-Xin Cheng, and Federico Capasso. Meta-optics achieves rgb-achromatic focusing for virtual reality. *Science Advances*, 7(5): eabe4458, 2021. 1
- [51] Jingyun Liang, Jiezhong Cao, Guolei Sun, Kai Zhang, Luc Van Gool, and Radu Timofte. Swinir: Image restoration using swin transformer. In *Proceedings of the IEEE/CVF international conference on computer vision*, pages 1833–1844, 2021. 2, 3, 4, 5
- [52] Jingyun Liang, Jiezhong Cao, Yuchen Fan, Kai Zhang, Rakesh Ranjan, Yawei Li, Radu Timofte, and Luc Van Gool. Vrt: A video restoration transformer. *IEEE Transactions on Image Processing*, 2024. 7, 8
- [53] Dianmin Lin, Pengyu Fan, Erez Hasman, and Mark L. Brongersma. Dielectric gradient metasurface optical elements. *Science*, 345(6194):298–302, 2014. 2, 3
- [54] Zin Lin, Charles Roques-Carmes, Raphaël Pestourie, Marin Soljačić, Arka Majumdar, and Steven G. Johnson. End-to-end nanophotonic inverse design for imaging and polarimetry. *Nanophotonics*, 10(3):1177–1187, 2021. 2
- [55] Hanzhou Liu, Binghan Li, Chengkai Liu, and Mi Lu. Deblurdinat: A lightweight and effective transformer for image deblurring, 2024. 3, 4
- [56] Pengju Liu, Hongzhi Zhang, Lian Wei, and Wangmeng Zuo. Multi-level wavelet convolutional neural networks. *IEEE Access*, 7:74973–74985, 2019. 2
- [57] Zhisheng Lu, Juncheng Li, Hong Liu, Chaoyan Huang, Linlin Zhang, and Tiejong Zeng. Transformer for single image super-resolution. In *Proceedings of the IEEE/CVF conference on computer vision and pattern recognition*, pages 457–466, 2022. 3, 6
- [58] Joseph N. Mait, Ravindra A. Athale, Joseph van der Gracht, and Gary W. Euliss. Potential applications of metamaterials to computational imaging. In *Proc. Frontiers in Optics / Laser Science*, page FTu8B.1, 2020. 2
- [59] Xiao-Jiao Mao, Chunhua Shen, and Yubin Yang. Image restoration using very deep convolutional encoder-decoder networks with symmetric skip connections. In *Neural Information Processing Systems*, 2016. 2
- [60] Ben Mildenhall, Pratul P. Srinivasan, Rodrigo Ortiz-Cayon, Nima Khademi Kalantari, Ravi Ramamoorthi, Ren Ng, and Abhishek Kar. Local light field fusion: Practical view synthesis with prescriptive sampling guidelines. *ACM Transactions on Graphics (TOG)*, 2019. 8, 16
- [61] Anish Mittal, Rajiv Soundararajan, and Alan C Bovik. Making a “completely blind” image quality analyzer. *IEEE Signal processing letters*, 20(3):209–212, 2012. 15
- [62] Naoki Murata, Koichi Saito, Chieh-Hsin Lai, Yuhta Takida, Toshimitsu Uesaka, Yuki Mitsufuji, and Stefano Ermon. Gibbsddrm: A partially collapsed gibbs sampler for solving blind inverse problems with denoising diffusion restoration. In *International conference on machine learning*, pages 25501–25522. PMLR, 2023. 2
- [63] A. Ndao, Li-Yi Hsu, Jeongho Ha, Junhee Park, C. Chang-Hasnain, and B. Kanté. Octave bandwidth photonic fishnet-achromatic-metalens. *Nature Communications*, 11:3205, 2020. 3
- [64] Joon-Suh Park, Shuyan Zhang, Alan She, Wei Ting Chen, Peng Lin, Kerolos MA Yousef, Ji-Xin Cheng, and Federico Capasso. All-glass, large metalens at visible wavelength using deep-ultraviolet projection lithography. *Nano letters*, 19(12):8673–8682, 2019. 1
- [65] S.M. Pizer, R.E. Johnston, J.P. Ericksen, B.C. Yankaskas, and K.E. Muller. Contrast-limited adaptive histogram equalization: speed and effectiveness. In *[1990] Proceedings of the First Conference on Visualization in Biomedical Computing*, pages 337–345, 1990. 15
- [66] Federico Presutti and Francesco Monticone. Focusing on bandwidth: achromatic metalens limits. *Optica*, 7(6):624–631, 2020. 3
- [67] Valeriya Pronina, Filippos Kokkinos, Dmitry V Dylov, and Stamatios Lefkimmiatis. Microscopy image restoration with deep wiener-kolmogorov filters. In *Computer Vision—ECCV 2020: 16th European Conference, Glasgow, UK, August 23–28, 2020, Proceedings, Part XX 16*, pages 185–201. Springer, 2020. 4
- [68] Kambiz Rahbar and Karim Faez. Blind correction of lens aberration using zernike moments. In *2011 18th IEEE International Conference on Image Processing*, pages 861–864. IEEE, 2011. 3
- [69] Christian J Schuler, Michael Hirsch, Stefan Harmeling, and Bernhard Schölkopf. Blind correction of optical aberrations. In *Computer Vision—ECCV 2012: 12th European Conference on Computer Vision, Florence, Italy, October 7–13, 2012, Proceedings, Part III 12*, pages 187–200. Springer, 2012. 3
- [70] Yan Shen, Ying Chen, Qing Liu, Shuqin Lou, Weidong Yu, Xinmin Wang, and Houjin Chen. Improved anscombe transformation and total variation for denoising of lowlight infrared images. *Infrared Physics & Technology*, 93:192–198, 2018. 15
- [71] Yichang Shih, Brian Guenter, and Neel Joshi. Image enhancement using calibrated lens simulations. In *Computer Vision—ECCV 2012: 12th European Conference on Computer Vision, Florence, Italy, October 7–13, 2012, Proceedings, Part IV 12*, pages 42–56. Springer, 2012. 3
- [72] Sajjan Shrestha, Adam C. Overvig, Ming Ying Lu, Aaron Stein, and Nanfang Yu. Broadband achromatic dielectric metalenses. *Light: Science & Applications*, 7:85, 2018. 3
- [73] Jiaming Song, Chenlin Meng, and Stefano Ermon. Denoising diffusion implicit models. *arXiv preprint arXiv:2010.02502*, 2020. 2, 3
- [74] Endri Stoja, Simon Konstandin, Dennis Philipp, Robin N Wilke, Diego Betancourt, Thomas Bertuch, Jürgen Jenne, Reiner Umathum, and Matthias Günther. Improving magnetic resonance imaging with smart and thin metasurfaces. *Scientific reports*, 11(1):16179, 2021. 1
- [75] Shuo Chen Su, Mauricio Delbracio, Jue Wang, Guillermo Sapiro, Wolfgang Heidrich, and Oliver Wang. Deep video deblurring for hand-held cameras. In *Proceedings of the IEEE conference on computer vision and pattern recognition*, pages 1279–1288, 2017. 7, 8, 15, 20
- [76] Shaolin Su, Qingsen Yan, Yu Zhu, Cheng Zhang, Xin Ge, Jinqiu Sun, and Yanning Zhang. Blindly assess image quality in the wild guided by a self-adaptive hyper network. In

- Proceedings of the IEEE/CVF conference on computer vision and pattern recognition*, pages 3667–3676, 2020. 15
- [77] Long Sun, Jiangxin Dong, Jinhui Tang, and Jinshan Pan. Spatially-adaptive feature modulation for efficient image super-resolution. In *ICCV*, 2023. 3, 4
- [78] Huixuan Tang and Kiriakos N Kutulakos. What does an aberrated photo tell us about the lens and the scene? In *IEEE International Conference on Computational Photography (ICCP)*, pages 1–10. IEEE, 2013. 3
- [79] Fu-Jen Tsai, Yan-Tsung Peng, Yen-Yu Lin, Chung-Chi Tsai, and Chia-Wen Lin. Stripformer: Strip transformer for fast image deblurring. In *ECCV*, 2022. 3
- [80] Ethan Tseng, Shane Colburn, James Whitehead, Luocheng Huang, Seung-Hwan Baek, Arka Majumdar, and Felix Heide. Neural nano-optics for high-quality thin lens imaging. *Nature communications*, 12(1):6493, 2021. 2, 3, 6, 7, 13, 15, 16
- [81] Zhijun Tu, Kunpeng Du, Hanting Chen, Hailing Wang, Wei Li, Jie Hu, and Yunhe Wang. Ipt-v2: Efficient image processing transformer using hierarchical attentions. *arXiv preprint arXiv:2404.00633*, 2024. 2, 3, 4, 5, 14
- [82] Shuming Wang, Pin Chieh Wu, Vin-Cent Su, Yi-Chieh Lai, Cheng Hung Chu, Jia-Wern Chen, Shen-Hung Lu, Ji Chen, Beibei Xu, Chieh-Hsiung Kuan, et al. Broadband achromatic optical metasurface devices. *Nature Communications*, 8(1):187, 2017. 3
- [83] Shuming Wang, Pin Chieh Wu, Vin-Cent Su, Yi-Chieh Lai, Mu-Ku Chen, Hsin Yu Kuo, Bo Han Chen, Yu Han Chen, Tzu-Ting Huang, Jung-Hsi Wang, Ray-Ming Lin, Chieh-Hsiung Kuan, Tao Li, Zhen lin Wang, Shining Zhu, and Din Ping Tsai. A broadband achromatic metalens in the visible. *Nature Nanotechnology*, 13:227–232, 2018. 3
- [84] Zhou Wang, Alan C Bovik, Hamid R Sheikh, and Eero P Simoncelli. Image quality assessment: from error visibility to structural similarity. *IEEE transactions on image processing*, 13(4):600–612, 2004. 15
- [85] Zhendong Wang, Xiaodong Cun, Jianmin Bao, Wengang Zhou, Jianzhuang Liu, and Houqiang Li. Uformer: A general u-shaped transformer for image restoration. In *Proceedings of the IEEE/CVF Conference on Computer Vision and Pattern Recognition (CVPR)*, pages 17683–17693, 2022. 3, 4
- [86] Norbert Wiener. *Extrapolation, interpolation, and smoothing of stationary time series: with engineering applications*. The MIT press, 1949. 2, 3, 4, 7, 16
- [87] Sidi Yang, Tianhe Wu, Shuwei Shi, Shanshan Lao, Yuan Gong, Mingdeng Cao, Jiahao Wang, and Yujiu Yang. Maniqa: Multi-dimension attention network for no-reference image quality assessment. In *Proceedings of the IEEE/CVF conference on computer vision and pattern recognition*, pages 1191–1200, 2022. 15
- [88] Gwanho Yoon, Kwan Kim, Se-Um Kim, Seunghoon Han, Heon Lee, and Junsuk Rho. Printable nanocomposite metalens for high-contrast near-infrared imaging. *ACS nano*, 15(1):698–706, 2021. 1
- [89] Nanfang Yu and Federico Capasso. Flat optics with designer metasurfaces. *Nature Materials*, 13:139–150, 2014. 2, 3
- [90] Tao Yue, Jinli Suo, Yudong Xiao, Lei Zhang, and Qionghai Dai. Image quality enhancement using original lens via optical computing. *Optics express*, 22(24):29515–29530, 2014. 3
- [91] Tao Yue, Jinli Suo, Jue Wang, Xun Cao, and Qionghai Dai. Blind optical aberration correction by exploring geometric and visual priors. In *Proceedings of the IEEE Conference on Computer Vision and Pattern Recognition*, pages 1684–1692, 2015. 3
- [92] Syed Waqas Zamir, Aditya Arora, Salman Khan, Munawar Hayat, Fahad Shahbaz Khan, Ming-Hsuan Yang, and Ling Shao. Multi-stage progressive image restoration. In *CVPR*, 2021. 2
- [93] Syed Waqas Zamir, Aditya Arora, Salman Khan, Munawar Hayat, Fahad Shahbaz Khan, and Ming-Hsuan Yang. Restormer: Efficient transformer for high-resolution image restoration. In *Proceedings of the IEEE/CVF conference on computer vision and pattern recognition*, pages 5728–5739, 2022. 2, 3, 4, 5, 6, 7, 14, 15, 16
- [94] Kai Zhang, Wangmeng Zuo, Shuhang Gu, and Lei Zhang. Learning deep cnn denoiser prior for image restoration. In *IEEE Conference on Computer Vision and Pattern Recognition*, pages 3929–3938, 2017. 2
- [95] Richard Zhang, Phillip Isola, Alexei A Efros, Eli Shechtman, and Oliver Wang. The unreasonable effectiveness of deep features as a perceptual metric. In *Proceedings of the IEEE conference on computer vision and pattern recognition*, pages 586–595, 2018. 15
- [96] Shuyan Zhang, Chi Lok Wong, Shuwen Zeng, Renzhe Bi, Kolvyn Tai, Kishan Dholakia, and Malini Olivo. Metasurfaces for biomedical applications: imaging and sensing from a nanophotonics perspective. *Nanophotonics*, 10(1):259–293, 2020. 1
- [97] Zhihong Zhang, Yuxiao Cheng, Jinli Suo, Liheng Bian, and Qionghai Dai. Infwide: Image and feature space wiener deconvolution network for non-blind image deblurring in low-light conditions. *IEEE Transactions on Image Processing*, 32:1390–1402, 2023. 3, 4
- [98] Guoxing Zheng, Holger Mühlenbernd, Mitchell Kenney, Guixin Li, Thomas Zentgraf, and Shuang Zhang. Metasurface holograms reaching 80% efficiency. *Nature Nanotechnology*, 10:308–312, 2015. 2
- [99] Yuqian Zhou, David Ren, Neil Emerton, Sehoon Lim, and Timothy Large. Image restoration for under-display camera. In *Proceedings of the IEEE/CVF conference on computer vision and pattern recognition*, pages 9179–9188, 2021. 4

Aberration Correcting Vision Transformers for High-Fidelity Metalens Imaging: Supplementary Materials

A. Metalens Fabrication

A.1. Fabrication Details

A metalens with a diameter of $500\ \mu\text{m}$ and a focal length of $1\ \text{mm}$ was designed based on the optimization of a polynomial phase equation [80]. The SiN meta-atom library was generated using rigorous coupled-wave analysis (RCWA) simulations for circular pillars with a height of $750\ \text{nm}$. The widths of the selected meta-atoms ranged from 100 to $300\ \text{nm}$, with a lattice period of $350\ \text{nm}$.

A $750\ \text{nm}$ thick SiN layer was deposited onto a SiO_2 substrate using plasma-enhanced chemical vapor deposition (PECVD; Oxford, PlasmaPro 100 Cobra) to fabricate the designed metalens. A $200\ \text{nm}$ thick positive photoresist layer (AR-P 6200.09, Allresist) was spin-coated at $4000\ \text{RPM}$. The pattern of circular nano-pillar meta-atoms was then transferred onto the positive photoresist using electron beam lithography, as shown in Fig. 13 (a), with a dose of $3.75\ \text{C}/\text{m}^2$. To prevent charging, $100\ \mu\text{L}$ of ESPACER (RESONAC, 300Z) was spin-coated at $2000\ \text{RPM}$ for $30\ \text{s}$.

The exposed resist was developed in a 1:3 solution of methyl isobutyl ketone (MIBK)/isopropyl alcohol (IPA) for $11\ \text{min}$. Subsequently, a $40\ \text{nm}$ thick chromium (Cr) layer was deposited as a hard mask using an electron beam evaporator (Fig. 13 (b)). The unexposed photoresist was removed through a lift-off process in acetone at room temperature for $1\ \text{hour}$, leaving the Cr hard mask intact. Patterning was finalized using inductively coupled plasma (ICP) etching (STS, multiplex ICP) with SF_6 ($15\ \text{sccm}$) and C_4H_8 ($40\ \text{sccm}$) gases for $10\ \text{min}$. Finally, the Cr hard mask was removed using a chromium etchant (TRANSENE, CE-905N) for $5\ \text{min}$. The fabricated metalens is illustrated in Fig. 14.

A.2. Optical Setup for Imaging

An image capture setup is illustrated in Fig. 15. An optical microscope system was set up to obtain images through the metalens. The images displayed on a 5.5 -inch FHD display (FeelWorld, LUT5) were captured using a CMOS camera (Allied Vision, Alvium 1800 U-235c) coupled with a magnification system consisting of a $20\times$ objective lens (Olympus, UPlanFL N 20x) with $0.5\ \text{NA}$ and a tube lens (Thorlabs, TTL180-A).

The metalens was positioned such that its focal plane coincided with the focal plane of the objective lens using a linear motorized stage (Thorlabs, DDS100). Camera exposure time was adjusted using a white image prior to recording to prevent saturation.

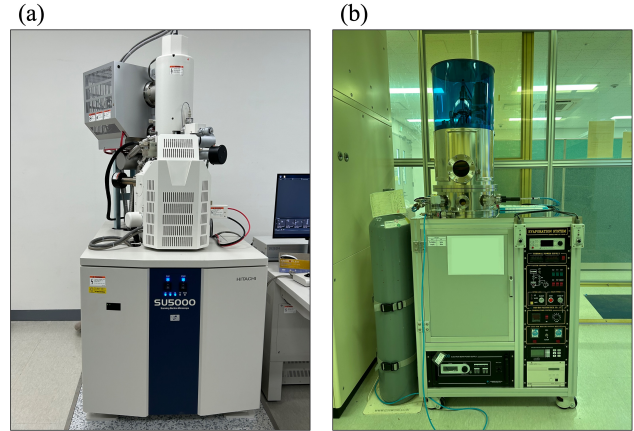


Figure 13. Equipments used for metalens fabrication. (a). Electron beam lithography system for high precision patterning of the metalens. (b). Electron beam evaporator to deposit a Cr layer as a hard mask during the fabrication process.

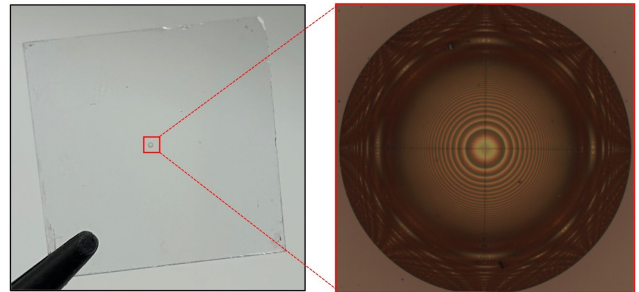


Figure 14. The fabricated metalens.

The point spread functions (PSFs) were then acquired using the same setup with $450\ \text{nm}$ laser (Thorlabs, CPS450), $532\ \text{nm}$ laser (Thorlabs, CPS532), and $635\ \text{nm}$ laser (Thorlabs, CPS635) for calibration and training of the model.

B. Analysis and Discussion

In this section, we provide a comprehensive analysis to demonstrate the effectiveness of the proposed methods. All models are trained with a quarter of the original batch size.

Effect of MAFG. To validate the effectiveness of MAFG, we conducted ablation studies on each module of MAFG as shown in Tab. 4, which compares MAFG and other two baselines. The first baseline (*MAFG w/o CA*) does not apply cross-attention to the deconvolved images but simply concatenates them and feeds the concatenated features to the restoration network, which drops PSNR by $0.28\ \text{dB}$. We

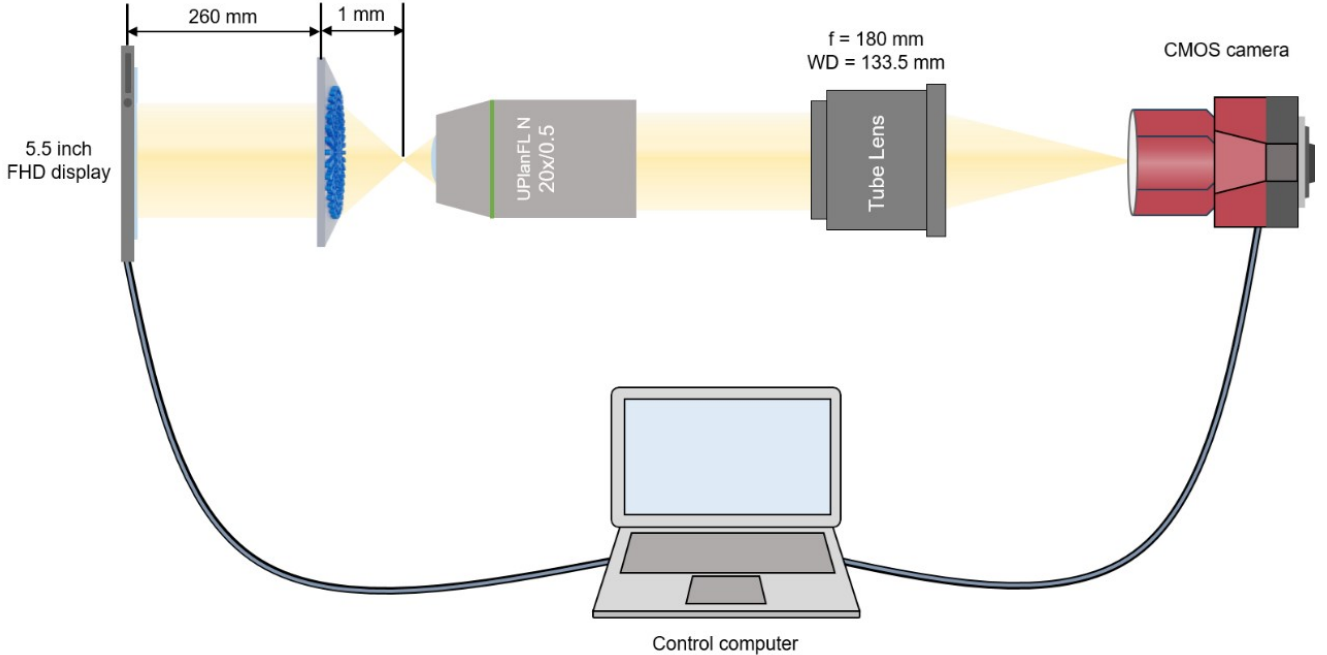


Figure 15. Experimental display imaging setup. The same setup was used to capture RGB PSFs.

Method	PSNR \uparrow	SSIM \uparrow	LPIPS \downarrow
MAFG w/o CA	33.59	0.8697	0.2044
MAFG w/o CI	33.82	0.8728	0.2074
MAFG	33.87	0.8757	0.2036

Table 4. Ablation study on the MAFG.

# filters	PSNR \uparrow	SSIM \uparrow	LPIPS \downarrow
3	33.60	0.8725	0.2027
7	33.76	0.8737	0.2040
13	33.87	0.8757	0.2036

Table 5. Ablation study on the number of filters of MAFG.

assume this is because cross-attention can reweight the deconvolved representations considering the degree of aberrations, proving it is proper to handle metalens images where aberration varies across the image. The other baseline (*MAFG w/o CI*) does not consider channel intensity when designing Wiener filters. Noise is signal-dependent (*e.g.* bright regions have more noise variance) and requires different noise regularization on different intensities, but this approach cannot reflect such property. It undermines perceptual quality, degrading LPIPS by 0.0038. We believe that a more sophisticated approach to incorporating image information into the filters can further improve the restoration quality. Lastly, Tab. 5 compares the number of filters M involved in MAFG. The more filters we employed, the aberration correction performance was improved as it could enrich the input of the restoration network more and reweight the features more adaptively. Thus, we use 13 different filters considering the memory.

Effect of STAF. Tab. 6 provides experimental results to demonstrate the competence of STAF. Employing transposed self-attention (TA) alone, similar to Restormer [93]

often lacks encoding spatial context, leading to the worst performance among the baselines (first row in Tab. 6). In the case of harnessing both spatial self-attention (SA) and TA, the way of fusing two different features also affects the restoration quality. Sequentially applying SA and TA (second row) where several previous works [12, 15, 81] proposed, still fall short of performance as SA and TA are identically implemented in both encoder and decoder. Meanwhile, the proposed STAF (fourth row) can effectively aggregate the outputs from two different modules considering the roles of encoder and decoder. It further facilitates restoration by enforcing queries of attention modules in decoder blocks focusing more on the fine details and achieves 0.18 dB improvement in PSNR compared to using original queries (third row), resulting in superior restoration quality.

C. Implementation Details

We trained our model for 100K iterations with a batch size of 8 on 4 RTX A6000 GPUs. We adopted Overlapping Cross Attention (OCA), which partitions query matrix with

Modules	Aggregation	QE	PSNR \uparrow	SSIM \uparrow	LPIPS \downarrow
TA	-	✓	33.07	0.8671	0.2062
SA, TA	Sequential	✓	33.63	0.8690	0.2165
SA, TA	Weighted sum		33.69	0.8714	0.2051
SA, TA	Weighted sum	✓	33.87	0.8757	0.2036

Table 6. Ablation study on the STAF.

non-overlapping windows and key and value matrices with overlapping windows, from HAT [14] for our SA module, following X-Restormer [12]. We employed the Gated-Deconv Feed-Forward network from Restormer [93] for our feed-forward network (FFN). Please refer to Restormer and X-Restormer for more details.

For the cross-attention module in the MAFG, we projected the deconvolved images to 32-dimensional feature space. The cross-attention uses overlapping windows similar to the SA modules in STAF and adopts two attention heads. In the case of image dataset construction, we resized each image such that the longer dimension (either height or width) was set to 1215 pixels, while the shorter dimension was scaled proportionally to fit the images to the sensor size while preserving the original aspect ratio. We set the sensor noise n in Eq. (1) in the main paper as a sum of Gaussian and Poisson noise. Each noise is sampled from the Gaussian distribution $\mathcal{N}(x, \sigma_g^2)$ and the Poisson distribution $\mathcal{P}(\frac{x}{\sigma_p})$, respectively, where x is the image, $\sigma_g = 1e - 5$, and $\sigma_p = 4e - 5$, following Tseng et al. [80].

D. Additional Results

In this section, we provide additional experimental results on each task that were not delivered in the main paper due to the page limit. We also attached videos of the 3D reconstruction and video aberration correction task results.

Evaluation Metrics We assessed the proposed method with various evaluation metrics including Peak Signal-to-Noise Ratio (PSNR), Structural Similarity Index Measure (SSIM) [84], and Learned Perceptual Image Patch Similarity (LPIPS) [95]. We further validated our methods with non-reference metrics, including Multi-scale Image Quality (MUSIQ) [35], Multi-dimension Attention Network Image Quality Assessment (MANIQA) [87], Hyper-network Image Quality Assessment HyperIQA [76] and Natural Image Quality Evaluator (NIQE) [61] on the image datasets.

D.1. Image Aberration Correction

Fig. 16 shows extra qualitative results on the Open Image V7 [6, 44] dataset with spatially variant aberration. The proposed method can mitigate aberrations in both central and peripheral regions and restore fine details. Tab. 7 shows the evaluations on non-uniform aberration datasets under several non-reference metrics, and the proposed method consistently outperforms diverse baseline models.

Method	MUSIQ \uparrow	MANIQA \uparrow	HyperIQA \uparrow	NIQE \downarrow
Restormer [93]	48.028	0.243	0.340	7.326
Restormer [93] + SWF	48.028	0.239	0.326	7.295
Ours	50.938	0.267	0.360	6.967

Table 7. Quantitative results on non-reference evaluation metrics.

We also provide additional results on five different uniform aberration datasets, where we used the PSFs at 0° , 5° , 10° , and 15° , 20° field angle, respectively. As shown in Fig. 17, Restormer [93] shows visually satisfactory results on the mildly aberrated dataset (0° and 5° field angle), revealing the potential of ViT in metalens imaging. However, both Restormer and Restormer with a single Wiener filter (Restormer + SWF) struggle with restoring fine details or lose image contrast when the images are harshly aberrated (15° and 20° field angle), highlighting sophisticated approach is required. Since the proposed method can model spatially variant aberration, it can also effectively correct uniform aberrations at various field angles.

D.2. Images from the Fabricated Metalens

Model Fine-tuning Details We fine-tuned our pre-trained model, from Sec. 3.4 in the main paper, using images captured with the fabricated metalens. The fine-tuning dataset includes 200 images for training and 20 images for validation. However, they appeared to be dark and exhibited significant noise. To mitigate these issues, we implemented a preprocessing pipeline from Shen et al. [70]. Specifically, we applied Contrast-Limited Adaptive Histogram Equalization (CLAHE) [65] to enhance contrast, utilized an improved Anscombe transformation in the wavelet domain, and performed total variation-based denoising before reconstructing the images.

We fine-tuned the pre-trained model for 5,500 iterations and the fine-tuned network could produce promising results, despite the limited dataset size.

Results Fig. 18 presents the qualitative results of images captured with the fabricated metalens and restored ones using the proposed method and other baseline models. All models are fine-tuned under the same experimental settings. The captured images are harshly degraded, but the proposed method could effectively restore the overall color fidelity of the images with fine details, while other baseline models produce noisy and low-contrast outputs. Such outcomes can demonstrate the adaptability of the proposed method to real-world scenarios.

D.3. Video Aberration Correction

Fig. 19 shows additional qualitative results on the aberrated DVD [75] dataset. Similar to Fig. 10 in the main paper, the proposed method could robustly address aberrations in the video and produce aberration corrected representations.

Method	Uniform aberration at $\theta = 5^\circ$			Uniform aberration at $\theta = 10^\circ$			Uniform aberration at $\theta = 15^\circ$		
	PSNR \uparrow	SSIM \uparrow	LPIPS \downarrow	PSNR \uparrow	SSIM \uparrow	LPIPS \downarrow	PSNR \uparrow	SSIM \uparrow	LPIPS \downarrow
Wiener deconvolution [86]	27.14	0.6653	0.4316	26.72	0.6455	0.4661	26.61	0.6479	0.4656
Eboli et al. [21]	20.75	0.5363	0.6560	20.36	0.5172	0.6909	19.40	0.4794	0.7512
DeblurGANv2 [43]	25.18	0.7286	0.3041	24.51	0.7025	0.3335	23.53	0.6599	0.4036
DWDN [19]	29.04	0.8256	0.2505	27.99	0.8010	0.2691	27.09	0.7763	0.2969
Tseng et al. [80]	29.91	0.8366	0.2513	29.59	0.8213	0.2587	29.14	0.8141	0.2701
Restormer [93]	30.21	0.8654	0.1956	31.51	0.8671	0.2045	30.98	0.8526	0.2202
Restormer [93] + SWF	33.07	0.8672	0.2227	32.10	0.8434	0.2504	31.21	0.8337	0.2630
Ours	34.83	0.8904	0.1795	34.39	0.8788	0.1979	34.05	0.8708	0.2070

Table 8. Quantitative results Open Image V7 [6, 44] dataset with spatially varying and invariant aberration, where θ denotes a field angle.

Method	PSNR \uparrow	SSIM \uparrow	LPIPS \downarrow
3D-GS [37]	19.58	0.3857	0.8166
3D-GS w/ Ours	25.88	0.6669	0.3696
3D-GS + Ours	25.94	0.6676	0.3693

Table 9. Quantitative results on the Mip-NeRF 360 [5] dataset with spatially varying aberration.

wild imaging. To address this limitation, we are designing a new lens optimized for real world applications, and propose a more robust and effective restoration network capable of handling metalens-captured scenes as a future work.

D.4. 3D Reconstruction with Aberrated Images

Implementation Details We set the loss weighting hyperparameter $\lambda = 1.0$ for the Tanks&Temples [40] datasets. For the LLFF [60] dataset, we set $\lambda = 0.75$ and inactivated periodically resetting opacity of 3D Gaussians to preserve more points in the forward-facing dataset [46]. We use default hyperparameters including learning rate, training iterations and 3D Gaussian densification parameters from the original paper [37] for our experiments.

Results We provide extra qualitative results on the LLFF [60] and Tanks&Temples [40] datasets in Fig. 20 and Fig. 21. We further conducted experiments on Mip-NeRF 360 [5] dataset with spatially varying aberration, where we set $\lambda = 1.0$. As described in Tab. 9, the proposed training pipeline that embed our pre-trained restoration network into 3D-GS could improve the scene reconstruction quality through additional multi-view consistency guidance. Fig. 22 shows that 3D-GS could not model the spatially varying aberration of metalens and failed to produce clean representations. On the other hands, the proposed method enables aberration modeling, demonstrating the capability of clean 3D reconstruction from the set of multi-view aberrated images of our approach.

E. Limitations and Future Work

We fabricated a metalens using the phase profile of [80] and captured images projected on the display, following its optical setup. However, capturing actual scenes can introduce various physical variables, such as multiple light sources and noises, which can undermine the quality of the images, but the current optical system is not well-suited for in-the-

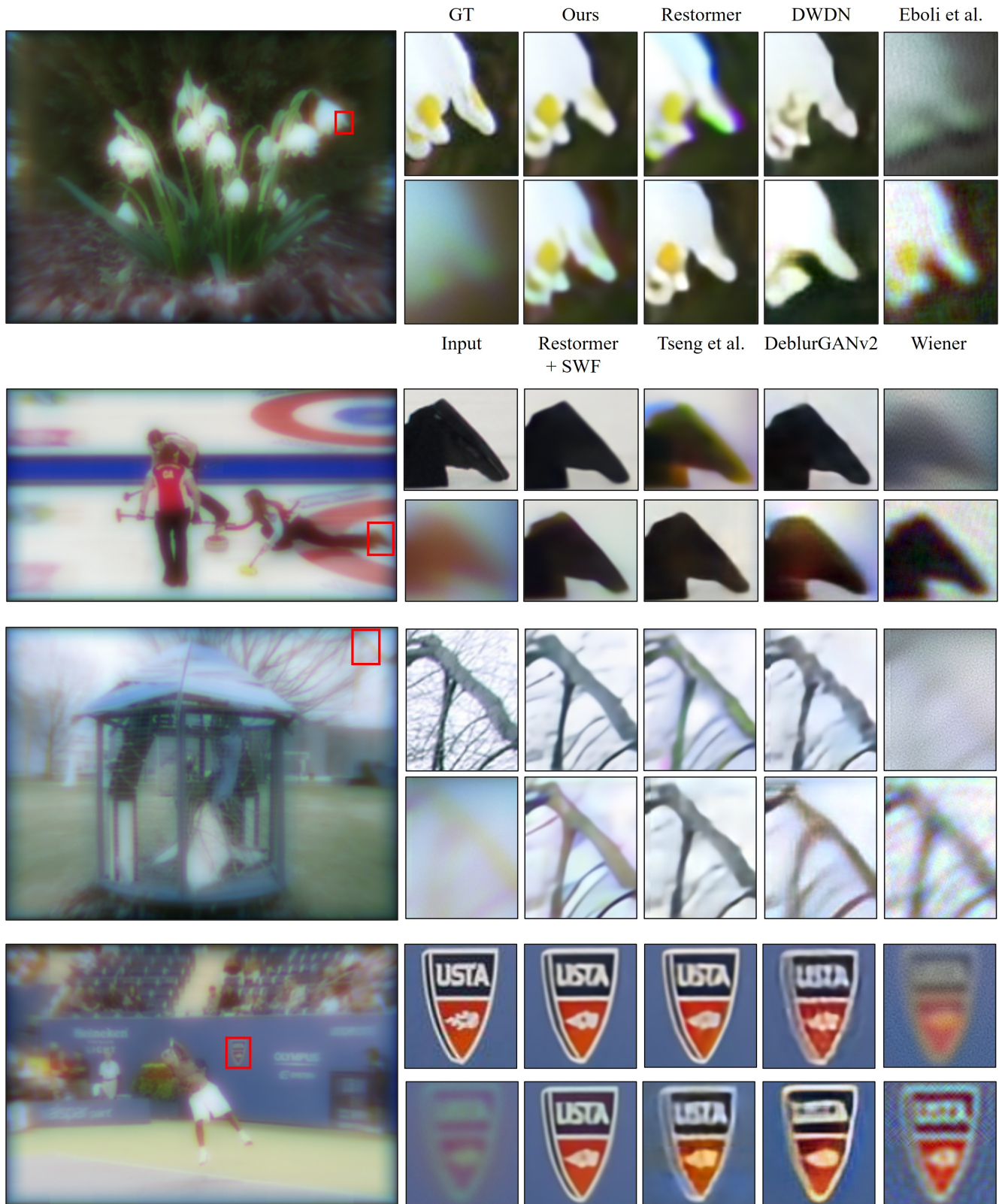


Figure 16. Additional qualitative results on the Open Image V7 [6, 44] dataset with spatially variant aberration.

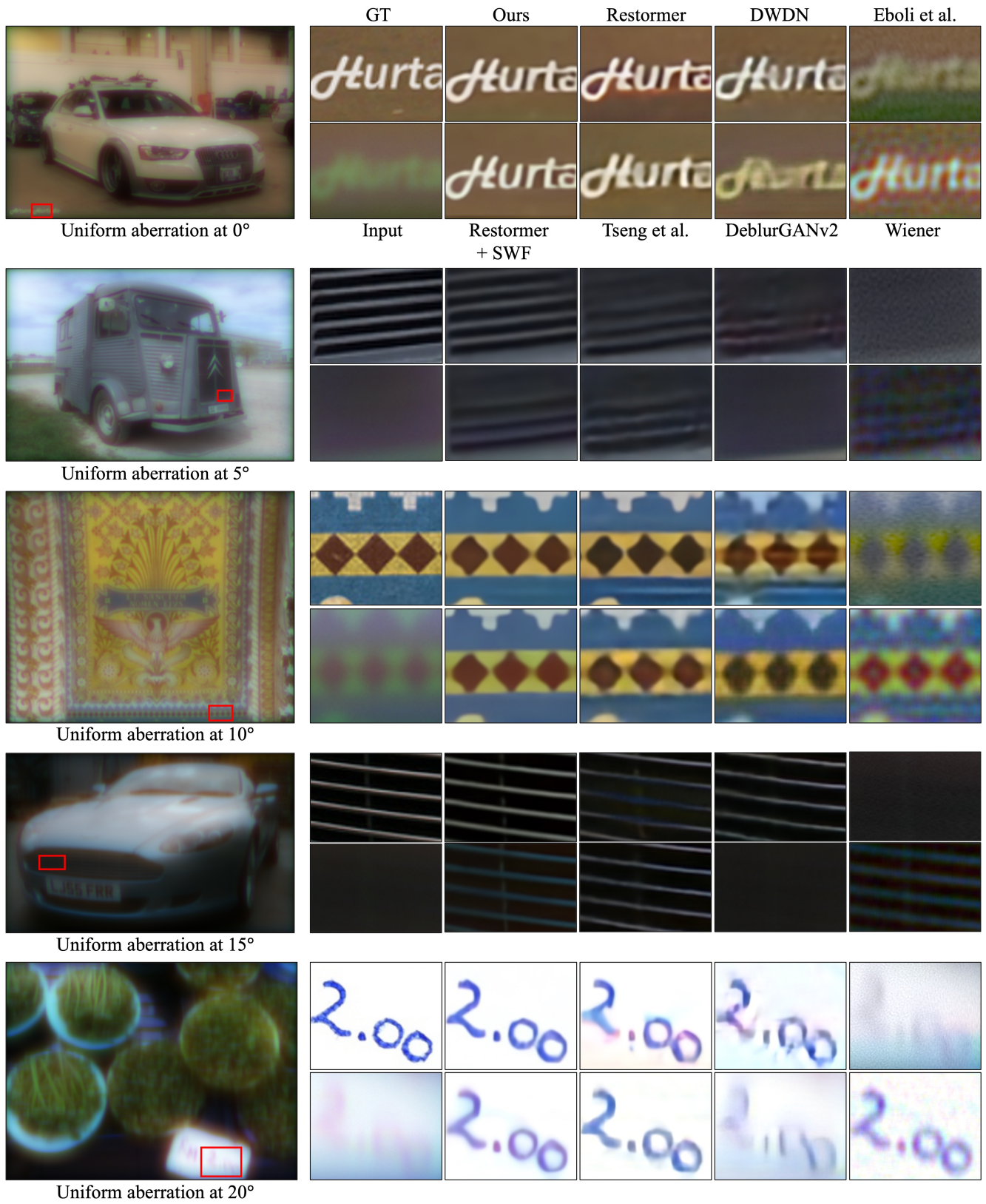


Figure 17. Additional qualitative results on the Open Image V7 [6, 44] dataset with uniform aberration at different field angles.

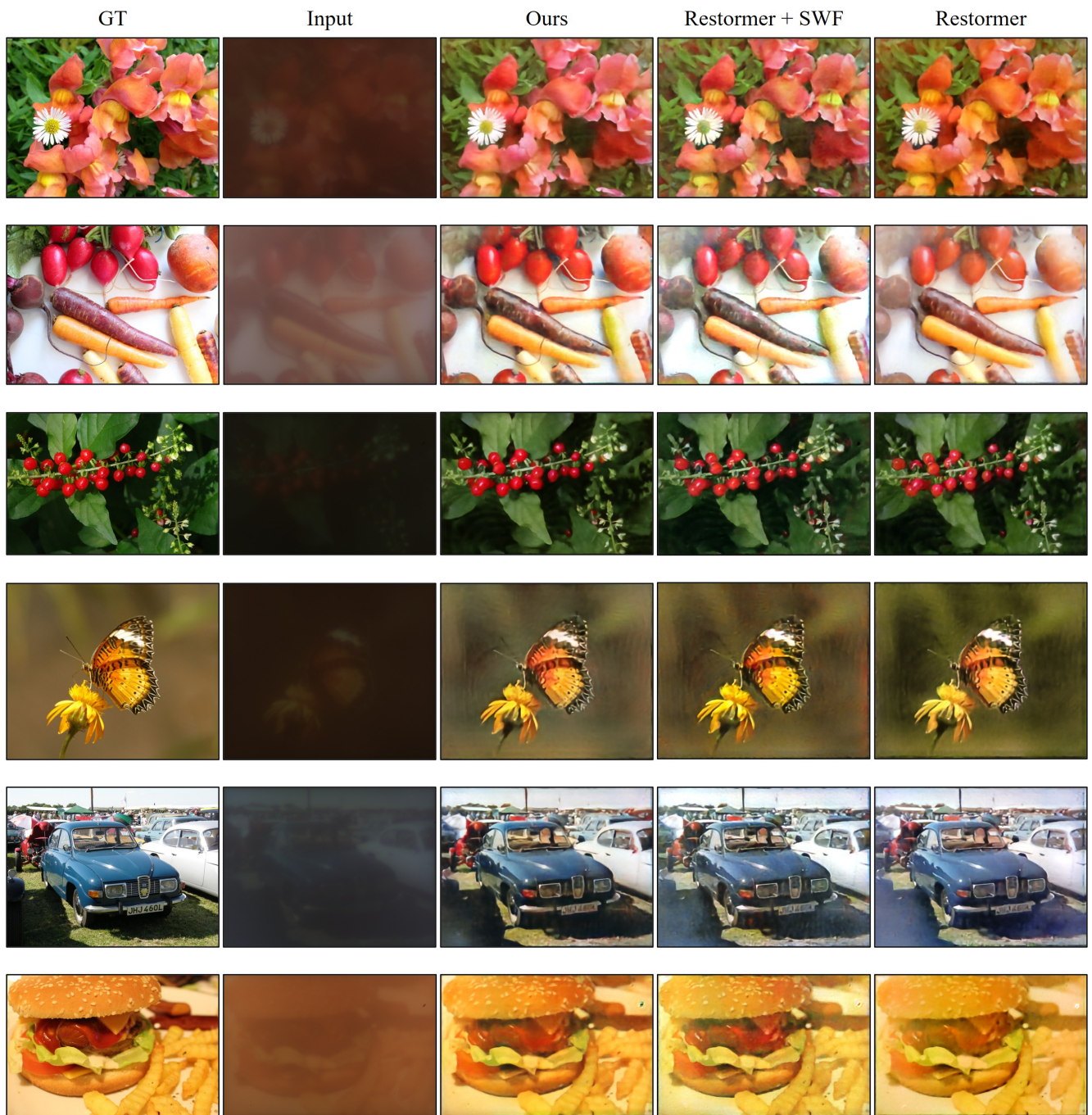


Figure 18. Additional qualitative results on the captured images with the fabricated metalens.

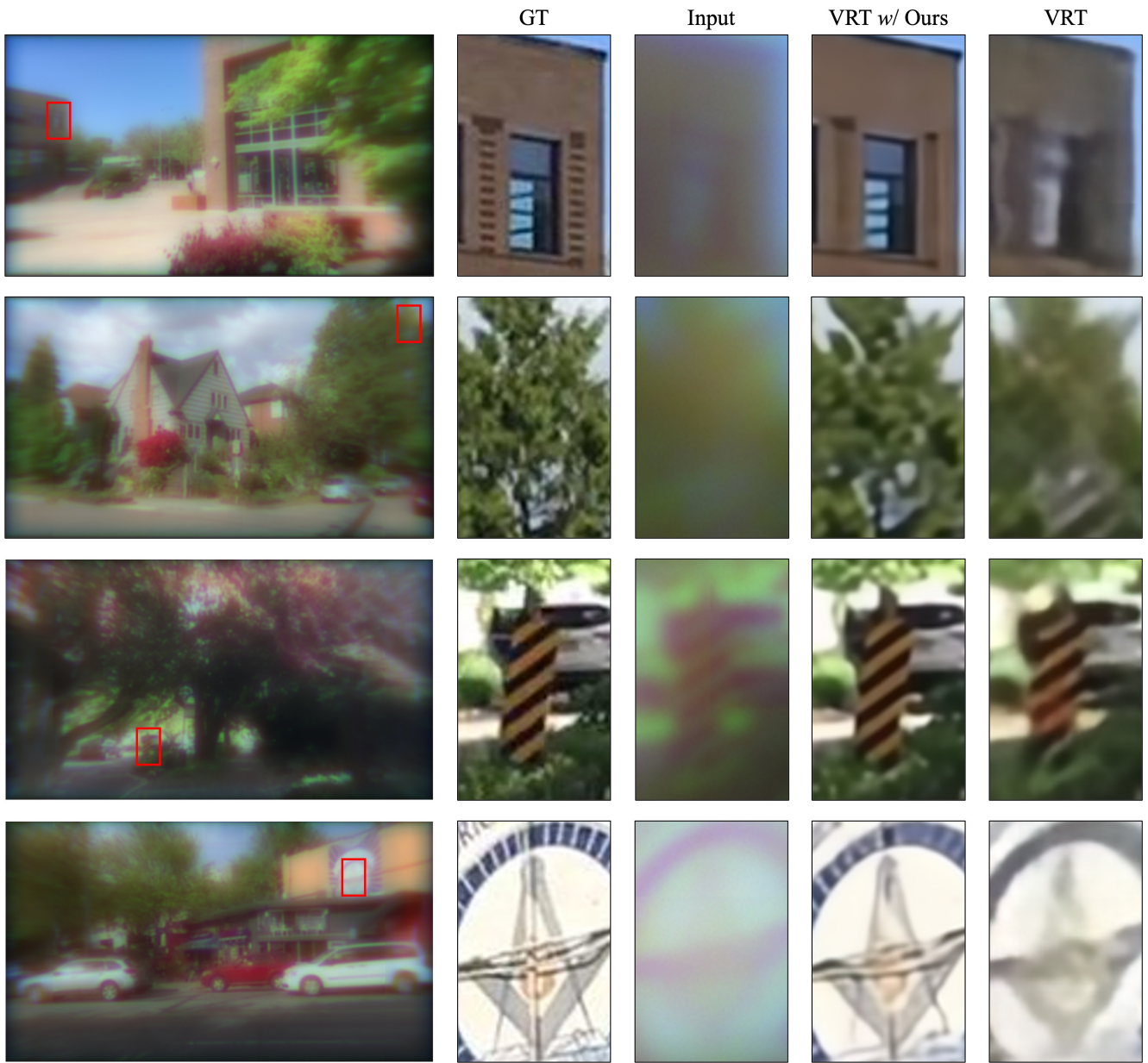
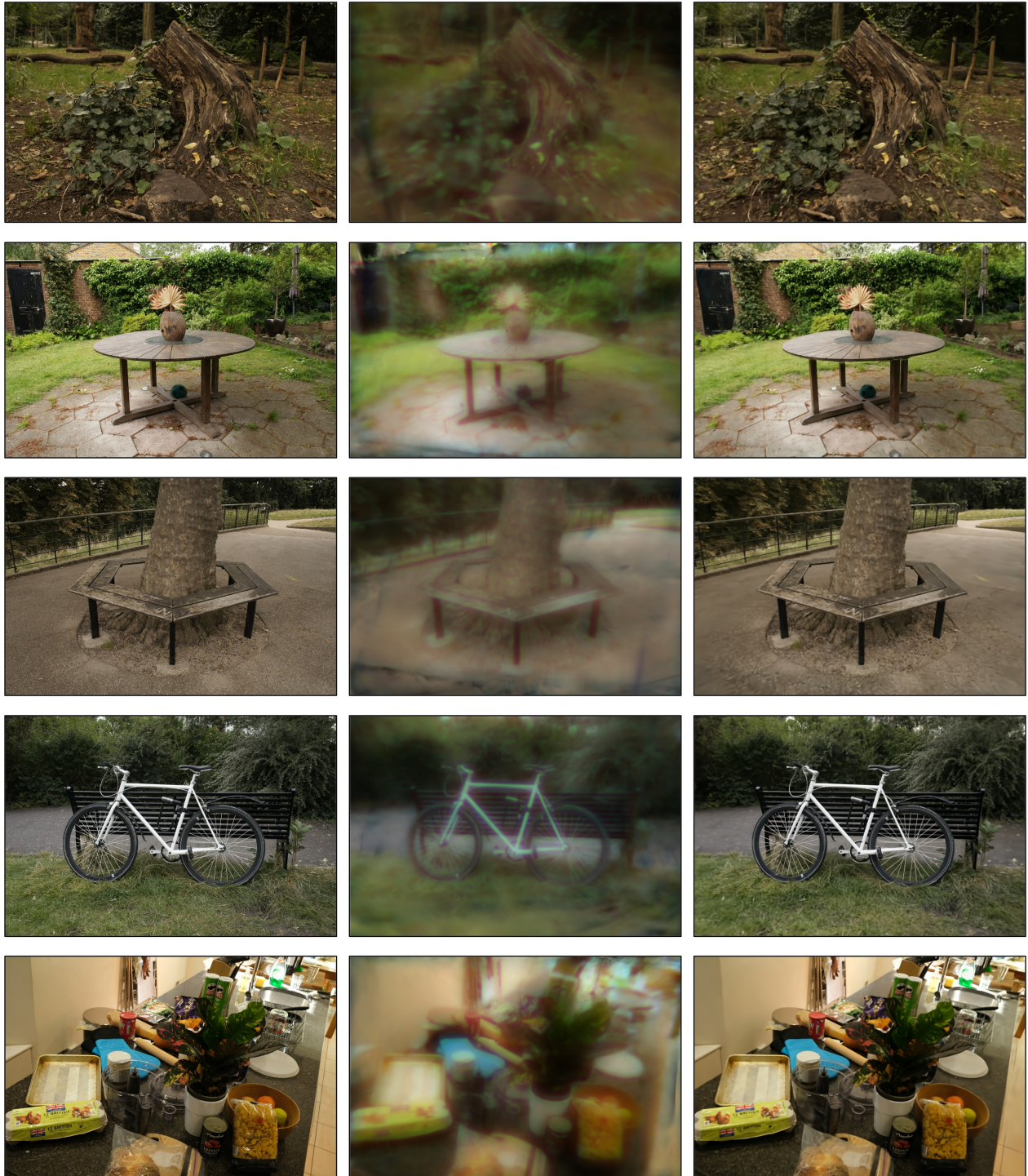


Figure 19. Additional qualitative results on the aberrated DVD [75] dataset.



GT

3D-GS

3D-GS + Ours

Figure 22. Qualitative results on the aberrated Mip-NeRF 360 [5] dataset.